



Hydrodynamic coupling of a cilia–mucus system in Herschel–Bulkley flows

Q. Mao¹, U. D’Ortona¹ and J. Favier^{1,†}

¹Aix-Marseille University, CNRS, Centrale Med, M2P2 Marseille, France

(Received 12 March 2024; revised 20 May 2024; accepted 15 July 2024)

The yield stress and shear thinning properties of mucus are identified as critical for ciliary coordination and mucus transport in human airways. We use here numerical simulations to explore the hydrodynamic coupling of cilia and mucus with these two properties using the Herschel–Bulkley model, in a lattice Boltzmann solver for the fluid flow. Three mucus flow regimes, i.e. a poorly organized regime, a swirly regime, and a fully unidirectional regime, are observed and analysed by parametric studies. We systematically investigate the effects of ciliary density, interaction length, Bingham number and flow index on the mucus flow regime formation. The underlying mechanism of the regime formation is analysed in detail by examining the variation of two physical quantities (polarization and integral length) and the evolution of the flow velocity, viscosity and shear-rate fields. Mucus viscosity is found to be the dominant parameter influencing the regime formation when enhancing the yield stress and shear thinning properties. The present model is able to reproduce the solid body rotation observed in experiments (Loiseau *et al.*, *Nat. Phys.*, vol. 16, 2020, pp. 1158–1164). A more precise prediction can be achieved by incorporating non-Newtonian properties into the modelling of mucus as proposed by Gsell *et al.* (*Sci. Rep.*, vol. 10, 2020, 8405).

Key words: pulmonary fluid mechanics

1. Introduction

Mucociliary clearance driven by ciliary beating in the human airways has received much attention due to its critical role in the capture and clearance of foreign pollutants and pathogens (Wanner, Salathé & O’Riordan 1996; Grotberg 2021; Sedaghat, Behnia & Abouali 2023). Human airways are protected by two fluid layers, a periciliary layer (PCL) covering the epithelial surface and a mucus layer on top of the PCL (Chilvers & O’Callaghan 2000; Knowles & Boucher 2002; Choudhury *et al.* 2023). The mucus is often described as a yield stress and shear thinning fluid (Banerjee, Bellare & Puniyani 2001; Nordgard & Draget 2011; Chatelin *et al.* 2017). Cilia are almost immersed in the PCL,

† Email address for correspondence: julien.favier@univ-amu.fr

and interact with the mucus through their tips. The force generated by the cilia propels the mucus flow, and the mucus in turn affects the orientation of the ciliary beating (Gsell *et al.* 2020; Loiseau *et al.* 2020; Pellicciotta *et al.* 2020). This hydrodynamic coupling between mucus and millions of microscopic cilia has a major impact on ciliary coordination (self-organization) and mucus transport. Understanding the hydrodynamic mechanism of cilia–mucus interaction is desirable for the study of various respiratory diseases caused by the impairment of mucus transport.

Considerable research effort has been devoted to the ciliary coordination and cilia-induced flow. For the former, the proposal of a cilia model can be traced back to an analytical study by Barton & Raynor (1967), where the cilium was simplified as an oscillating cylinder mounted on a plate. The relationship between the flow rate and the geometric parameters of the cilium was determined. Since then, many other studies involving modelling flexible cilia have been reported. Two asymmetric beating phases of a cilium were identified, i.e. an effective stroke characterized by almost straight cilium to better drive the mucus, and a recovery stroke characterized by large deformed cilium to reduce the retarding effect on the mucus (Blake 1972; Xu & Jiang 2019). Cilia in an array can coordinate with each other to generate metachronal waves instead of repeating two beating phases synchronously (Husson, Breugem & Westerweel 2011; Elgeti & Gompper 2013; Meng *et al.* 2021; Mesdjian *et al.* 2022; Wang, Tang & Zhang 2022). This usually depends on the phase difference between adjacent cilia (Chateau *et al.* 2017; Hall & Clarke 2020), and is related to ciliary flexibility (Kim & Netz 2006) and ciliary density (Chateau *et al.* 2018). Various metachronal waves have been observed, such as the antiplectic and symplectic waves. These two waves move in the opposite and same directions as the flow, respectively. Cilia beating with an antiplectic wave were found to be more efficient in transporting and mixing fluid than cilia beating synchronously or with a symplectic wave. On the other hand, various experimental and numerical studies have investigated the cilia-induced flow, usually focusing on local flow characteristics and flow rate (Brumley *et al.* 2014; Wei *et al.* 2019, 2021; Boselli *et al.* 2021; Hu & Meng 2023). Among them, Brumley *et al.* (2014) measured the flow around a single cilium and a pair of cilia, and calculated the instantaneous forces generated by the cilia using a Stokeslet model. They highlighted the importance of hydrodynamic coupling; a synchronized beating of two cilia can be realized even when only hydrodynamic interactions exist. Furthermore, Ding *et al.* (2014) observed a transport region and a mixing (shear) region above and below the ciliary tips, respectively. The asymmetric stroke of the cilia and the no-slip epithelial surface resulted in a shear-like flow field. The enhancement of fluid transport and mixing was mainly attributed to the increase in the shear rate. Fluid transport was also found to be continuous even though the epithelial surface was not completely covered by the cilia (Juan *et al.* 2020).

A long-range ciliary coordination distinct from metachronal waves has been discovered (Matsui *et al.* 1998; Tarran *et al.* 2005; Shapiro *et al.* 2014; Khelloufi *et al.* 2018), characterized by large-scale mucus swirls accompanied by cilia beating in a circular pattern. Several experimental studies have shown the existence of hydrodynamic coupling between the ciliary coordination and the circular mucus flow (Mitchell *et al.* 2007; Guirao *et al.* 2010; Faubel *et al.* 2016). Recently, Loiseau *et al.* (2020) and Gsell *et al.* (2020) experimentally investigated the hydrodynamic coupling of the cilia–mucus system in detail, and proposed a two-dimensional model to predict the ciliary coordination and the Newtonian mucus flow. They demonstrated that the hydrodynamic coupling of cilia and mucus dominates the long-range coordination. The formation of mucus swirls was closely related to the density and the interaction length of the cilia. As mentioned above, mucus is a non-Newtonian fluid with yield stress and shear thinning properties. Some

researchers have investigated the effect of non-Newtonian properties on mucus transport (Chatelin & Poncet 2016; Sedaghat, George & Abouali 2021; Sedaghat *et al.* 2022; Modaresi 2023; Wang *et al.* 2023). The present study aims to focus first on the yield stress and shear thinning properties, although the mucus rheology also exhibits other properties, e.g. viscoelasticity (Vasquez *et al.* 2016; Guo & Kanso 2017; Choudhury *et al.* 2023). Most of the studies employed numerical methods because the non-Newtonian properties can be well controlled. However, few studies have been reported on the effect of non-Newtonian properties on long-range ciliary coordination, which warrants a more detailed investigation.

The objective of the present study is to explore numerically the hydrodynamic coupling of cilia and mucus with yield stress and shear thinning properties. The mucus flow is solved by the lattice Boltzmann method. The cilia–mucus interaction is handled by an alignment rule, and the non-Newtonian fluid is modelled by the Herschel–Bulkley model. The effects of ciliary density (ϕ), interaction length (λ), Bingham number (Bn , quantifying yield stress effect) and flow index (n , quantifying shear thinning effect) on the formation of the mucus flow (or ciliary beating orientation) regime are examined. Three different mucus flow regimes are observed: a poorly organized (PO) regime, a swirly (S) regime, and a fully unidirectional (FU) regime (corresponding to the poorly aligned, swirly and fully aligned regimes in Gsell *et al.* 2020). Two physical parameters, i.e. polarization (P) and integral length (Λ), are used to identify the three regimes. The mechanism of regime formation caused by the yield stress and shear thinning effects is characterized by the evolution of the flow velocity, viscosity and shear-rate fields. In addition, a rescaling of λ is proposed for different Bn and n .

2. Computational model

Mucus flow is almost parallel to the epithelium and uniform along the direction perpendicular to the epithelium (Gsell *et al.* 2020). In addition, we concentrate on long-range fluid flow parallel to the epithelium, whose length scale is much larger than the typical fluid layer thickness. Therefore, the mucus flow is considered to be two-dimensional, and a two-dimensional hydrodynamic model is sufficient to describe the mucus motion. The flow is predicted based on a lattice Boltzmann solver, and the interaction between the ciliary beating and the mucus motion is handled by an alignment rule. A visualization of the computational domain for $\phi = 0.3$ is shown in figure 1(a). The square domain is approximately $160D$ in both length and height. The cells are discretized using hexagonal elements, where the ciliated elements (black) are randomly placed during initialization. A hexagonal element represents a patch containing several ciliated cells with a common direction of ciliary beating. Approximately 10^4 elements are contained in the domain. Here, D represents the side length of the hexagonal elements, and $\phi = A_c/A$ represents the ciliary density, where A_c is the ciliated area, and A is the total area. A closer visualization of the hexagonal elements and the underlying lattice nodes is shown in figure 1(b). The computational domain is discretized on a uniform Cartesian grid. The black and grey dots represent ciliated and non-ciliated nodes, respectively. Note that cilia are simplified as ciliated nodes. Ciliary beating is modelled by a force that is constant in magnitude, whose orientation can change over time (Gsell *et al.* 2020). The initial condition is $\mathbf{u} = 0$, with random orientation of ciliary forces and random placement of ciliated elements. Periodic boundary conditions are specified at the domain boundaries.

In the lattice Boltzmann method (Krüger *et al.* 2017; Ma *et al.* 2020; Lu *et al.* 2022), the particle distribution function $f(\mathbf{x}, \boldsymbol{\xi}, t)$ is used to describe the mucus motion, representing

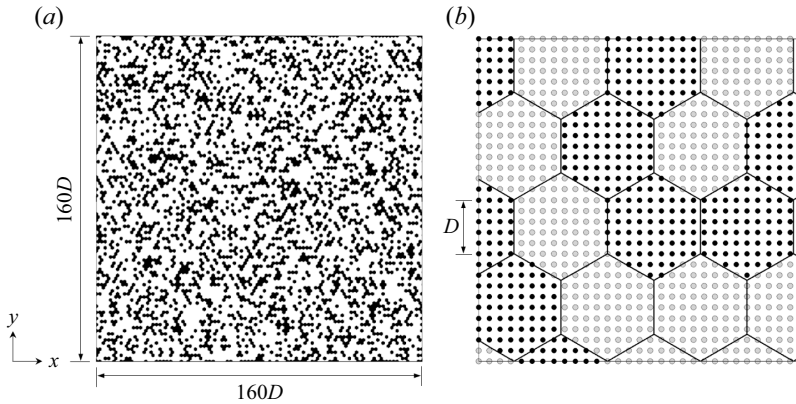


Figure 1. (a) Visualization of the computational domain (ciliary density $\phi = 0.3$). Cells are discretized using hexagonal elements, with ciliated elements (black) randomly placed during initialization. (b) Closer visualization of the hexagonal elements and the underlying lattice nodes. The black and grey dots represent ciliated and non-ciliated nodes, respectively.

the density of fluid particles moving with velocity ξ at location x and time t . The dynamics of $f(x, \xi, t)$ is governed by the Boltzmann equation:

$$\frac{\partial f}{\partial t} + \xi \cdot \nabla f = \Gamma(f), \tag{2.1}$$

where Γ is the collision operator. Equation (2.1) is equivalent to the Navier–Stokes equations at the macroscopic level (Krüger *et al.* 2017). The lattice Boltzmann equation is obtained by discretizing (2.1) in velocity space, physical space and time. A set of velocity vectors $\{e_l, l = 0, \dots, Q - 1\}$ is used to discretize the velocity space, where Q is the number of discrete velocities. The $D2Q9$ scheme is employed as the discretization model to discretize the velocity space by nine velocities:

$$e_l = \begin{cases} (0, 0), & l = 0, \\ c \left(\cos \left(\frac{\pi(l-1)}{2} \right), \sin \left(\frac{\pi(l-1)}{2} \right) \right), & l \in [1, 4], \\ \sqrt{2}c \left(\cos \left(\frac{\pi(2l-9)}{4} \right), \sin \left(\frac{\pi(2l-9)}{4} \right) \right), & l \in [5, 8], \end{cases} \tag{2.2}$$

where $c = \Delta x / \Delta t = \Delta y / \Delta t$ is the lattice velocity. As mentioned before, the computational domain is discretized on a uniform Cartesian grid, i.e. $\Delta h = \Delta x = \Delta y$ and $\Delta h = \Delta t = D/5 = 1$. The lattice Boltzmann equation is written as follows, normalizing all the quantities by c and Δt , and introducing an external body force:

$$f_i(x + e_l, t + 1) - f_i(x, t) = \Gamma_l(x, t) + S_l^*(x, t), \tag{2.3}$$

where $S_l^*(x, t)$ is the external body force term. The left- and right-hand sides of (2.3) are the streaming and collision steps, respectively. These two steps can be treated separately due to the explicit (2.3). A two-relaxation-time collision operator is used in the present

study:

$$\Gamma_l = -\frac{1}{\tau^+} (f_l^+ - f_l^{eq+}) - \frac{1}{\tau^-} (f_l^- - f_l^{eq-}), \quad (2.4)$$

where τ^+ and τ^- are the symmetric and antisymmetric relaxation times, and f_l^+ and f_l^- are the symmetric and antisymmetric parts of f_l . The kinematic fluid viscosity $\nu = c_s^2(\tau^+ - \frac{1}{2})$ is determined by τ^+ , where $c_s = 1/\sqrt{3}$ is the lattice sound speed, and τ^- is determined by the parameter $\Lambda_\tau = (\tau^+ - 0.5)(\tau^- - 0.5)$, where Λ_τ is kept constant to ensure the viscosity independence (Gsell, D’Ortona & Favier 2021), set to 1/4 according to the previous study (Ginzburg, d’Humières & Kuzmin 2010). Also, f_l^{eq} is the equilibrium particle distribution function, expressed as

$$f_l^{eq}(\mathbf{x}, t) = w_l \rho \left[1 + \frac{\mathbf{e}_l \cdot \mathbf{u}}{c_s^2} + \frac{(\mathbf{e}_l \cdot \mathbf{u})^2}{2c_s^4} - \frac{\mathbf{u}^2}{2c_s^2} \right], \quad (2.5)$$

where w_l are the lattice weights, and ρ is the fluid density. In the present $D2Q9$ scheme, $w_0 = 4/9$, $w_l = 1/9$ for $l = 1, \dots, 4$, and $w_l = 1/36$ for $l = 5, \dots, 8$ (Qian, d’Humières & Lallemand 1992). The symmetric and antisymmetric parts of f_l and f_l^{eq} are expressed as

$$\begin{cases} f_l^+ = \frac{f_l + \bar{f}_l}{2}, & f_l^- = \frac{f_l - \bar{f}_l}{2}, \\ f_l^{eq+} = \frac{f_l^{eq} + \bar{f}_l^{eq}}{2}, & f_l^{eq-} = \frac{f_l^{eq} - \bar{f}_l^{eq}}{2}, \end{cases} \quad (2.6)$$

where the index \bar{l} is defined such that $c_{\bar{l}} = -c_l$. The external body force term S_l^* is expressed as

$$S_l^* = \left(1 - \frac{1}{2\tau^+}\right) S_l^+ + \left(1 - \frac{1}{2\tau^-}\right) S_l^-, \quad (2.7)$$

where $S_l^+ = (S_l + S_{\bar{l}})/2$ and $S_l^- = (S_l - S_{\bar{l}})/2$ are the symmetric and antisymmetric parts of S_l , which is given as

$$S_l = w_l \left[\frac{\mathbf{e}_l \cdot \mathbf{u}}{c_s^2} + \frac{(\mathbf{e}_l \cdot \mathbf{u})\mathbf{e}_l}{c_s^4} \right] \mathbf{F}. \quad (2.8)$$

The macroscopic quantities ρ and \mathbf{u} are moments of the particle functions in the velocity space (Krüger *et al.* 2017), where ρ is expressed as

$$\rho = \sum_{l=0}^8 f_l. \quad (2.9)$$

The flow momentum corrected by the external forcing is

$$\rho \mathbf{u} = \sum_{l=0}^8 f_l \mathbf{e}_l + \frac{1}{2} \mathbf{F}, \quad (2.10)$$

where the forcing \mathbf{F} is the sum of the force \mathbf{F}_c exerted by the cilia and the frictional force \mathbf{F}_v generated by the PCL. We impose \mathbf{F}_c on the ciliated nodes only. In the present study,

we are interested in the long-term dynamics of the flow, i.e. in time scales that are much larger than the ciliary beating period. Therefore, time-dependent beating is simplified to a point force. Its magnitude is the same for all ciliated nodes and is constant over time, while its orientation is determined by the alignment rule during the simulation. In addition, F_c is assumed to be independent of mucus properties, e.g. viscosity of the mucus. The orientation of F_c is the same for the ciliated nodes in the same hexagonal element. In the present study, the magnitude of F_c is set to be the same as that of F_v during the initialization. The frictional force is proportional to the fluid velocity ($F_v = -\kappa u$), and the PCL is assumed to be a Newtonian fluid, where κ is the PCL friction coefficient. The frictional force is treated implicitly, and (2.10) becomes (Gsell *et al.* 2020)

$$\rho u = \frac{\sum_{l=0}^8 f_l e_l + \frac{1}{2} F_c}{1 + \kappa/2\rho}. \tag{2.11}$$

Recall that the orientation θ_c^j of F_c on the j th ciliated cell is determined by the alignment rule, which was inspired by certain experimental observations. The daily variations of the flow pattern of cilia-driven cerebrospinal fluid have been observed in *in vivo* mouse brain ventricles (Faubel *et al.* 2016). In addition, Guirao *et al.* (2010) showed that ciliary-beat orientations on cell cultures issued from the subventricular zone of newborn mice could be changed drastically by applying an external flow. The directional collective order of ciliary beats on the multiciliated skin cells of the *Xenopus* embryo could also be refined by applying an external flow to skin explants (Mitchell *et al.* 2007). Recently, it has been found that the directions of ciliary beating in human airways tend to align progressively along mucus streamlines (Gsell *et al.* 2020; Loiseau *et al.* 2020). A maximum angle reorientation of 35° – 40° was shown. The direction of ciliary beating is stable over time and does not show reorientation when mucus was washed out. The reorientation of the cilia is not related to the motility of the cells because the tissue is jammed and the turnover of epithelial cells is very slow. These phenomena strongly suggest the existence of a coupling between hydrodynamics and long-range ciliary-beat orientation, inspiring the present alignment rule. Here, $\Delta\theta = \theta_f^j - \theta_c^j$ represents the angle difference between the local flow (θ_f^j) and the ciliary beating (θ_c^j). The flow velocity is averaged over the j th ciliated cell. The alignment rule is expressed as

$$\theta_c^j(t + \Delta t) = \begin{cases} \theta_c^j(t) + \Omega \frac{\Delta\theta^j(t)}{|\Delta\theta^j(t)|} \Delta t, & \Delta\theta^j(t) > \theta_0, \\ \theta_c^j(t), & \Delta\theta^j(t) \leq \theta_0, \end{cases} \tag{2.12}$$

where Ω is a fixed angular velocity used to drive the reorientation of the ciliary beating, which does not affect the final steady solution (Gsell *et al.* 2020). Its value is $\Omega = U_0/D$, where $U_0 = 0.01$ is the reference velocity (in lattice units). Here, θ_0 is the angle threshold set to allow the steady solutions, i.e. $\theta_c^j(t + \Delta t) = \theta_c^j(t)$ when $\Delta\theta^j(t) \leq \theta_0$. The value of θ_0 is very small ($\theta_0 = 2\Omega \Delta t = 0.004$) to ensure a negligible influence on the final solutions. In summary, a two-way hydrodynamic coupling between the ciliary-beat orientation and the mucus motion is realized by the external forcing scheme and the alignment rule.

Hydrodynamic coupling of a cilia–mucus system

The Herschel–Bulkley model is employed to simulate non-Newtonian flows. The dynamic fluid viscosity μ is shear-dependent and is expressed as

$$\mu = \frac{\sigma_0}{\dot{\gamma}} + K\dot{\gamma}^{n-1}, \quad (2.13)$$

where σ_0 is the yield stress, K is the flow consistency, and n is the flow index. When $n < 1$, the viscosity decreases with increasing shear rate (shear thinning behaviour). When $n > 1$, the viscosity increases with increasing shear rate (shear thickening behaviour). In the present study, only the shear thinning behaviour is investigated. Here, $\dot{\gamma}$ is the local shear-rate magnitude, which is expressed as

$$\dot{\gamma} = \sqrt{2(S_{11}^2 + 2S_{12}^2 + S_{22}^2)}, \quad (2.14)$$

where $S_{\alpha\beta}$ is the local shear-rate tensor, expressed as

$$S_{\alpha\beta} = -\frac{1}{2\rho c_s^2 \tau^+} \left(\sum_{l=0}^8 (f_l - f_l^{eq}) e_{l\alpha} e_{l\beta} + \frac{1}{2} (u_\alpha F_\beta + u_\beta F_\alpha) \right), \quad (2.15)$$

where τ^+ is time-dependent in non-Newtonian simulations. According to $\nu = c_s^2(\tau^+ - 1/2)$ and (2.13), τ^+ is updated by

$$\tau^+ = \frac{\sigma_0 \dot{\gamma}^{-1} + K \dot{\gamma}^{n-1}}{\rho c_s^2} + \frac{1}{2}. \quad (2.16)$$

To avoid excessive viscosities during simulations, and to improve the numerical stability, the Herschel–Bulkley law is truncated. The maximum value of relaxation time τ_{max}^+ is 50, and the viscosity ratio μ_{max}/μ_{min} is 1000. A minimum $\dot{\gamma}$ is set as 10^{-14} to avoid zero $\dot{\gamma}$ in the simulation. As this threshold may seem arbitrary, a larger threshold (10^{-5}) was tested. The contours of viscosity and shear rate are very similar to those when the threshold is 10^{-14} , and the conclusions are unchanged. The viscosity will diverge as the shear rate approaches zero. However, this is reasonable since the mucus is a yield stress fluid. The reader is referred to Gsell *et al.* (2021) and Galko *et al.* (2022) for more details on the Herschel–Bulkley model.

The present model relies on five non-dimensional physical parameters, i.e. the ciliary density ϕ , the interaction length λ , the Reynolds number $Re = \rho U_0 D / \mu_0$ (where μ_0 is the reference viscosity), the Bingham number Bn , and the flow index n . Here, λ is defined as

$$\lambda = \frac{\sqrt{\mu_0/\kappa}}{D}. \quad (2.17)$$

A high mucus viscosity favours the diffusion of momentum caused by the ciliary beating while a high PCL friction coefficient κ prevents it. Thus λ represents the typical range of influence of the ciliated cells (Gsell *et al.* 2020). The flow of mucus is caused by the momentum transferred from the tip of the cilia. The momentum diffuses over a larger fluid region when λ is high. As mentioned previously, mucus flow is almost uniform and parallel to the epithelium. It can be assumed reasonably that no shear exists in the vertical direction for the present model. A reference shear rate can be defined as $\dot{\gamma}_0 = U_0/D$. The

Ciliary density (ϕ)	0.7–0.8 (Staudt <i>et al.</i> 2014)
Dynamic viscosity of the PCL (μ_p) Pa s	10^{-3} (Button <i>et al.</i> 2012)
Thickness of the PCL (δ_p) m	10^{-5} (Button <i>et al.</i> 2012)
Side length of a ciliated element (D) m	2×10^{-5} (Loiseau <i>et al.</i> 2020)
Viscosity of the healthy mucus (μ) Pa s	5×10^{-3} – 5×10^{-2} (Loiseau <i>et al.</i> 2020)
Yield stress of the mucus (σ_0) Pa	0.05 (Jory <i>et al.</i> 2022)
Flow index of the mucus (n)	0.15 (Jory <i>et al.</i> 2022)
Flow consistency of the mucus (K)	0.28 (Jory <i>et al.</i> 2022)
Normal velocity of the mucus (U_0) m s $^{-1}$	1.783×10^{-4} (Morgan <i>et al.</i> 2004)

Table 1. Experimental measurements of physical properties.

reference viscosity is $\mu_0 = K\dot{\gamma}_0^{n-1}$. The general definition of Re becomes (Gsell *et al.* 2021)

$$Re = \frac{\rho U_0^{2-n} D^n}{K}, \tag{2.18}$$

where $Re = 0.1$ is fixed to prevent inertial effects. Here, K can be obtained from (2.18), and Bn is defined as

$$Bn = \frac{\sigma_0}{K} \left(\frac{D}{U_0} \right)^n, \tag{2.19}$$

where the value of σ_0 is determined by Bn and can be obtained from (2.19).

The ranges of ϕ , λ , Bn and n are physiological and inspired by experimental measurements. Table 1 shows the experimental measurements of physical properties of the mucus. During the ciliogenesis in experiments (Loiseau *et al.* 2020), ciliary density increases from 0 to a value approximately 0.7–0.8 (normal ciliary density in the airway (Staudt *et al.* 2014)). In the present study, ϕ varies in the range $0.1 \leq \phi \leq 0.7$. From dimensional analysis, the PCL friction coefficient is $\kappa \approx \mu_p/\delta_p^2$, where μ_p and δ_p are the dynamic viscosity and thickness of the PCL; $\mu_p \approx 10^{-3}$ Pa s and $\delta_p \approx 10^{-5}$ m are obtained from Button *et al.* (2012). Also, $D \approx 2 \times 10^{-5}$ m and $\mu \approx 5 \times 10^{-3}$ – 5×10^{-2} Pa s (the viscosity of the healthy mucus) are obtained from Loiseau *et al.* (2020). Therefore, λ varies approximately in the range $1 \leq \lambda \leq 4$. Yield stress $\sigma_0 \approx 0.05$ Pa, averaged flow index $n \approx 0.15$ and flow consistency $K \approx 0.28$ are obtained and derived from Jory *et al.* (2022). The normal mucus velocity U_0 is approximately 1.783×10^{-4} m s $^{-1}$ (Morgan *et al.* 2004). Therefore, Bn is approximately 0.128, which is very close to the critical Bn (0.15) in the present study for the transition to the FU regime when $\phi = 0.7$. In the present study, Bn varies in the range $0 \leq Bn \leq 0.3$, enabling the observation of the transition to the FU regime for a very low ciliary density ($\phi = 0.1$). In the present study, n varies in the range $0.3 \leq n \leq 1$, which is sufficient to observe the transition to the FU regime for a very low ciliary density. Details of the regime transition will be discussed latter. Values $Bn = 0$ and $n = 1$ represent a Newtonian case.

Approximately 4500 simulations were performed to produce the results. The general procedure of the present numerical algorithm for the simulation of a coupled cilia–mucus system in Herschel–Bulkley flows can be summarized as follows (where the time march loop is performed until the steady solution is obtained). (i) At the n th time step, calculate the angular difference $\Delta\theta^j$ and update the orientation θ_c^j of F_c by (2.12). (ii) Perform the

collision step on the right-hand side of (2.3). Update the value of the relaxation time τ^+ by (2.16). (iii) Perform the streaming step on the left- side of (2.3) to obtain the new f_i . (iv) Calculate the new mucus density ρ and mucus velocity \mathbf{u} by (2.9) and (2.11). Update the value of the frictional force F_v .

3. Results and discussion

3.1. Mucus flow regimes of the cilia–mucus system

In the present study, three distinct mucus flow regimes are observed: a PO regime, an S regime and an FU regime. Figure 2(a) shows the contours of non-dimensional vorticity ($\omega_z = (D/U_0) |\nabla \times \mathbf{u}|$) of the three regimes for different λ and ϕ for a Newtonian fluid ($Bn = 0$, $n = 1$), where vectors indicate the direction of ciliary beating (local flow). The results in figures 2(a) and 4 obtained by the present model are almost the same as those obtained by Gsell *et al.* (2020). The PO regime is characterized by short-range coordination between adjacent cilia without the appearance of large-scale flow structures. The S regime is characterized by long-range coordination of cilia with the formation of obvious mucus swirls. In addition, the FU regime is characterized by long-range coordination of cilia with almost unidirectional flows. These three regimes have been observed in experiments of Loiseau *et al.* (2020). The PO regime corresponds to the pattern in their figures 1(c–e). The S regime corresponds to the pattern characterized by a small swirl (their figures 1f–h). The FU regime corresponds to the pattern characterized by a large swirl that occupies the entire culture chamber (their figure 1i), which is caused by the closed culture chamber. The appearance of the unidirectional flow in the present FU regime is attributed mainly to the periodic boundary condition.

To examine the formation of the three regimes for different λ and ϕ ($Bn = 0$, $n = 1$), the sequential processes of regime evolution from the initial state to the final steady state are plotted in figure 3. The contours are coloured by the non-dimensional flow velocity U/U_0 . Figure 3(a) shows the formation of the PO regime when λ and ϕ are very small ($\lambda = 1$ and $\phi = 0.1$). At instant a_1 , the domain is initialized with zero flow velocity, random ciliary-beat orientation and random cilia distribution. Mucus flow around the cilia is driven by the ciliary beating, visible at instant a_2 . The momentum caused by a ciliated element decays rapidly in space due to the small λ . The ciliated elements are scattered with large distances due to the small ϕ . Accordingly, the mucus flow caused by different cilia can interact with each other only if they are adjacent, resulting in several local flows without a typical flow structure at instant a_3 . The flow velocity in the PO regime is very low.

The S regime is formed when ϕ is large, as shown in figure 3(b). Mucus flows induced by ciliated elements have the same extension ($\lambda = 1$). However, as the ciliary density is higher, the coordination with neighbouring ciliated elements is improved, and the flow is organized over a greater distance. Several high-velocity regions are observed at instant b_2 due to the constructive interaction between the adjacent mucus flows. A uniform flow is not formed due to the low λ . At instant b_3 , swirls appear after a longer period of coordination than the local flows in the PO regime.

The FU regime is obtained when λ is increased, as shown in figure 3(c). The momentum generated by a ciliated element can propagate over a much greater distance. First, at instant c_2 , swirls are formed quickly due to the rapidly diffused mucus flows. Beyond c_2 , the further diffused mucus flows influence the ciliary beating over a larger area. After a long period of coordination, the cilia are almost aligned in the same direction, inducing a unidirectional and uniform flow at instant c_3 .

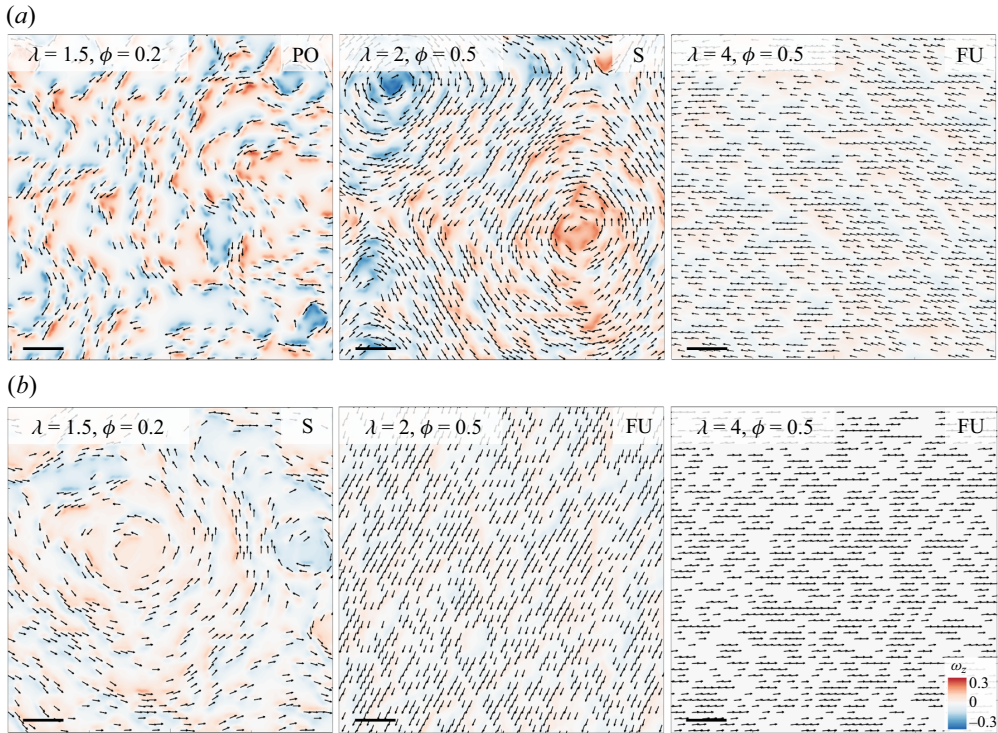


Figure 2. Final steady contours of non-dimensional vorticity ω_z (vectors indicate ciliary beating direction, and the colour bar indicates the magnitude of the vorticity) for (a) Newtonian fluid (Bingham number $Bn = 0$, flow index $n = 1$), and (b) non-Newtonian fluid ($Bn = 0.05$, $n = 0.9$). Three different mucus flow regimes are shown: PO regime, S regime and FU regime. Part of the computational domain is shown, and the scale bars correspond to $10D$.

3.2. Effects of ciliary density and interaction length

To quantitatively identify the PO, S and FU regimes in a wide range of parameters, two physical quantities are employed according to the characteristics of the three regimes. The first quantity is the polarization P used to identify the FU regimes, which is the spatial averaging of the unitary velocity vectors, expressed as

$$P = \left| \frac{\langle \mathbf{u} \rangle}{|\langle \mathbf{u} \rangle|} \right|, \tag{3.1}$$

where $P \approx 1$ represents a unidirectional flow. In the present study, $P \geq 0.9$ indicates the FU regime. This critical value is selected based on the observation that P increases sharply from a value below 0.6 to a value above 0.9 when the FU regime appears. This will be discussed in more detail later. The second quantity is the non-dimensional integral length Λ normalized by the dimensional interaction length $\sqrt{\mu/\kappa}$:

$$\Lambda = \sqrt{\frac{\kappa}{\mu}} \int_0^{L/2} \frac{R_x(\tau) + R_y(\tau)}{2} d\tau, \tag{3.2}$$

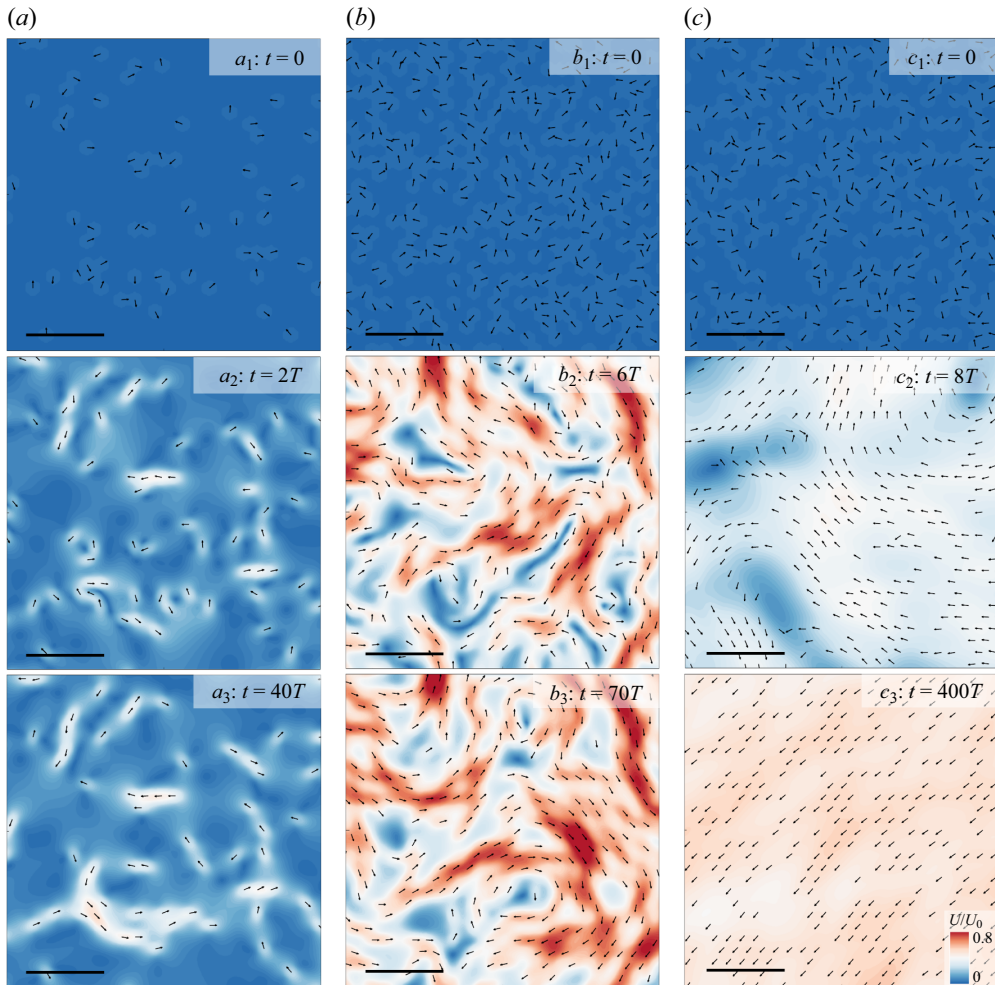


Figure 3. The sequential processes of evolution of the different mucus flow regimes ($Bn = 0$, $n = 1$, $T = 250 \Delta t$): (a) PO regime for $\lambda = 1$ (interaction length) and $\phi = 0.1$; (b) S regime for $\lambda = 1$ and $\phi = 0.5$; and (c) FU regime for $\lambda = 4$ and $\phi = 0.5$. Instantaneous contours of the non-dimensional velocity U/U_0 are shown. Part of the computational domain is shown, and the scale bars correspond to $10D$.

where L is the length of the computational domain, and $R_x(\tau)$ and $R_y(\tau)$ are the x and y components of the autocorrelation functions of the vorticity, respectively:

$$R_x(\tau) = \frac{\overline{\omega_z(x, y) \omega_z(x + \tau, y)}}{\overline{\omega_z^2}}, \quad (3.3)$$

$$R_y(\tau) = \frac{\overline{\omega_z(x, y) \omega_z(x, y + \tau)}}{\overline{\omega_z^2}}. \quad (3.4)$$

For $\tau > L/2$, the values of $R_x(\tau)$ and $R_y(\tau)$ are very small, except when τ approaches L because of the periodic boundary condition. Therefore, the domain of integration is $\tau \in [0, L/2]$ in (3.2). Here, Λ represents the length scale of flow structures. In particular, the length scale of flow structures is equivalent to the range of influence of the ciliated

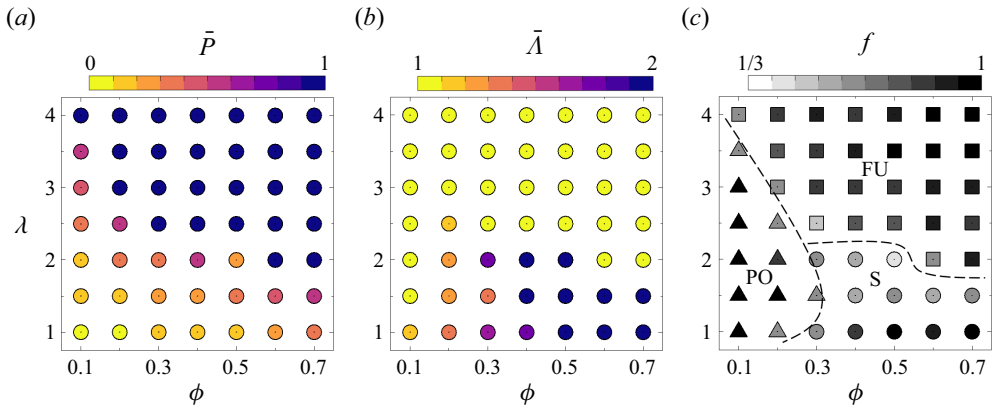


Figure 4. Mucus flow regime diagram depending on λ and ϕ for $Bn = 0$ and $n = 1$. Symbols are coloured using the values of (a) averaged polarization \bar{P} , (b) averaged integral length $\bar{\Lambda}$, and (c) occurrence frequency f of the mucus flow regime. The triangle, circle and square symbols correspond to PO, S and FU regimes, respectively.

cells when $\Lambda = 1$. Small and large Λ indicate the PO and S regimes, respectively. The increase in Λ is relatively smooth as the PO regime transitions to the S regime. The critical value $\Lambda = 1.5$ is selected based on the observation of the flow regime from numerous simulations. In summary, $P < 0.9$ and $\Lambda < 1.5$ indicate the PO regime, $P < 0.9$ and $\Lambda \geq 1.5$ indicate the S regime, and $P \geq 0.9$ indicates the FU regime.

For comparison, we first examine the effects of λ and ϕ on the formation of the mucus flow regime in the Newtonian case ($Bn = 0$, $n = 1$). Figure 4 shows a phase diagram in the ranges $1 \leq \lambda \leq 4$ and $0.1 \leq \phi \leq 0.7$. Random initialization can result in different flow regimes under certain conditions. Therefore, for each case in the diagram, 20 randomly initialized simulations were performed. Here, f is the occurrence frequency of the most frequent flow regime over a set of 20 simulations, and \bar{P} and $\bar{\Lambda}$ are the averaged polarization and integral length calculated by the simulations converged to the most frequent flow regime. In figure 4(a), symbols are coloured by the value of \bar{P} , which increases with increasing λ and ϕ . In figure 4(b), symbols are coloured by the value of $\bar{\Lambda}$. For $\bar{P} \geq 0.9$ (FU regime), $\bar{\Lambda}$ is set to be 1 and has no physical meaning. We do not discuss the length scale of the flow structures for the FU regime because it is theoretically infinite; $\bar{\Lambda}$ increases with ϕ . The effect of λ is less clear, but a small tendency of increasing $\bar{\Lambda}$ with decreasing λ may be observed. In figure 4(c), symbols are coloured by the value of f . The diagram is divided into three regions by dashed lines according to the maps of \bar{P} and $\bar{\Lambda}$. The PO regime appears in the region with low λ and ϕ . The S regime appears in the region with low λ and high ϕ . The FU regime appears in the region with high λ and high ϕ . As mentioned for figure 3, these are determined mainly by the range of influence of the ciliated cells and the interaction of the mucus flows caused by adjacent cilia; f is relatively small for the points near the regime boundary.

3.3. Effects of yield stress and shear thinning properties

For studying the effects of non-Newtonian properties on the flow regime formation, a phase diagram in the ranges $1 \leq \lambda \leq 4$ and $0.1 \leq \phi \leq 0.7$ is shown in figure 5. The simulated mucus is shear thinning, $n = 0.9$, and has a yield stress $Bn = 0.05$. The regions

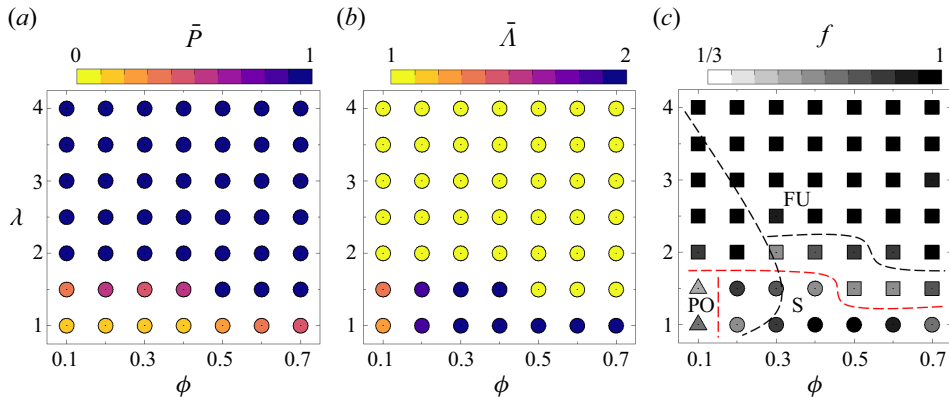


Figure 5. Mucus flow regime diagram depending on λ and ϕ for $Bn = 0.05$ and $n = 0.9$. Symbols are coloured using the values of (a) \bar{P} , (b) $\bar{\Lambda}$, and (c) f . The red and black dashed lines represent the boundaries of the non-Newtonian cases ($Bn = 0.05$, $n = 0.9$) and the Newtonian cases ($Bn = 0$, $n = 1$), respectively.

with high \bar{P} and low $\bar{\Lambda}$ are significantly enlarged compared to those for $Bn = 0$ and $n = 1$, as shown in figures 5(a,b). Figure 5(c) clearly shows the displacement of the regime boundary, where the red and black dashed lines represent the boundaries of the non-Newtonian cases ($Bn = 0.05$, $n = 0.9$) and the Newtonian cases ($Bn = 0$, $n = 1$), respectively. In general, the regions of the PO and S regimes are reduced, and the region of the FU regime is increased. The PO regime appears only when λ and ϕ are very low. The S regime is obtained at lower λ , while it appears in a wider range of ϕ . A lower λ allows the activation of the FU regime. The boundary between the PO and FU regimes is significantly changed. These indicate that the flow regimes of all cases can be converted to the FU regime by varying Bn and n . The point with $\phi = 0.1$ and $\lambda = 1$ would be the last case to complete this conversion. The flow regime of three non-Newtonian cases is shown in figure 2(b), which shows a significant regime transition when compared with the Newtonian cases in figure 2(a).

Here, we further examine the effects of Bn and n on the flow regime formation in detail. First, $n = 1$ is fixed to explore the effect of Bn independently, i.e. a Herschel–Bulkley fluid reduces to a Bingham fluid. In figure 6(a), the value of \bar{P} is presented with respect to the Bingham number Bn . Recall that to obtain the value of \bar{P} , only the simulations in the most frequent regime have been used. Thus each curve represents two sets of data that can be considered independently, and the sharp transition indicates the critical value of Bn that induces a transition to the FU regime. In the PO & S regime, \bar{P} increases monotonously with Bn , except for the case $\phi = 0.7$, where the variation is less clear. After the transition to the FU regime, \bar{P} remains almost constant. In general, a larger ϕ leads to a larger \bar{P} , confirming the results in figures 4(a) and 5(a). The critical Bn increases and then decreases with increasing ϕ , resulting in a maximum critical Bn at $\phi = 0.3$. In figure 6(b), the variation of $\bar{\Lambda}$ as a function of Bn is shown. The FU regime is not included due to its theoretically infinite length scale of the flow structures. $\bar{\Lambda}$ increases with increasing Bn for different ϕ . A larger ϕ leads to a larger $\bar{\Lambda}$, confirming the results in figures 4(b) and 5(b). For $\phi = 0.1$, a transition from the PO regime to the S regime is observed by increasing Bn . For $\phi > 0.1$, only the S regime is obtained. The above results suggest that the range of influence of the ciliated cells is increased by increasing Bn .

Figure 7 shows the variations of \bar{P} and $\bar{\Lambda}$ as functions of n for different ϕ , with $\lambda = 1$ and $Bn = 0$ fixed. The sharp increase of \bar{P} in figure 7(a) indicates the critical value of n

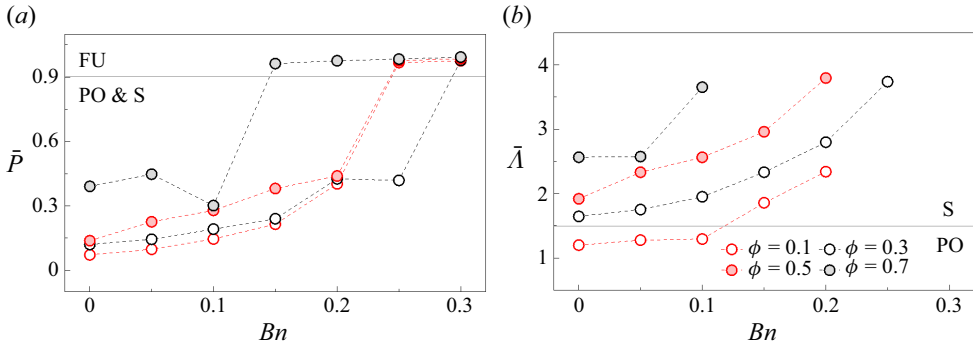


Figure 6. Values of (a) \bar{P} and (b) $\bar{\Lambda}$ as functions of Bn , for different ϕ ($\lambda = 1, n = 1$).

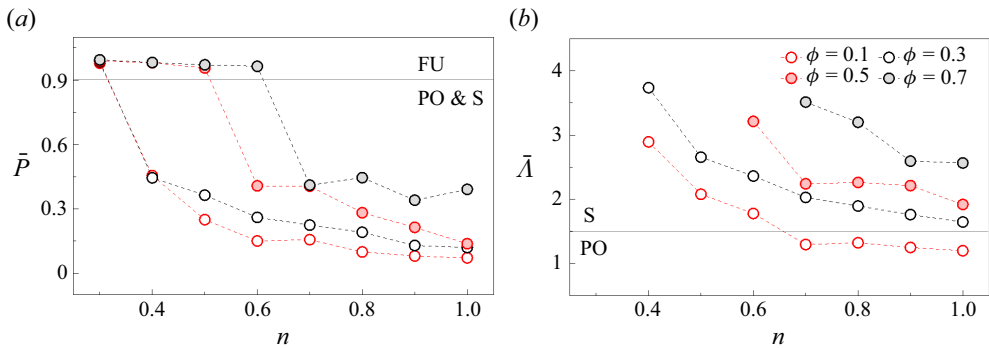


Figure 7. Values of (a) \bar{P} and (b) $\bar{\Lambda}$ as functions of n , for different ϕ ($\lambda = 1, Bn = 0$).

that leads to a transition to the FU regime. The critical n increases with increasing ϕ . In contrast to the effect of Bn , \bar{P} increases monotonously with decreasing n in the PO & S regime. After the transition to the FU regime, \bar{P} remains almost constant. In figure 7(b), the decrease of n can also lead to a transition from the PO regime to the S regime when the ciliary density is low ($\phi = 0.1$). The above results suggest that the range of influence of the ciliated cells is increased by decreasing n .

To visualize the transition from the PO regime to the S regime by increasing Bn , we further examine the instantaneous contours of the flow velocity U/U_0 , the dynamic fluid viscosity μ , and the local shear-rate magnitude $\dot{\gamma}$, by increasing Bn from 0 to 0.15 in figure 8 ($\lambda = 1, \phi = 0.1, n = 1$). Note that the steady solution for $Bn = 0$ (instant a_1) is used as the initial condition for the simulation with $Bn = 0.15$. A steady solution for $Bn = 0.15$ is obtained at instant a_2 . In figure 8(a), swirls are more pronounced at instant a_2 , corresponding to the increase in Λ from 6.36 to 10.99. This is caused mainly by the evolution of the μ and $\dot{\gamma}$ distributions in figures 8(b,c). At instant a_1 , μ is close to its reference value, and $\dot{\gamma}$ caused by the ciliary beating is high. At instant a_2 , μ in the region with low shear rate significantly increases with increasing Bn (yield stress). This can be verified by checking (2.13). The momentum diffuses farther when the viscosity is high. Accordingly, the mucus flow caused by a ciliated element affects the ciliary-beat orientation further away, which favours the coordination of the cilia, thereby resulting in a transition from the PO regime to the S regime. A reorientation of the cilia can be observed clearly in figure 8(a). However, the high viscosity makes the mucus difficult to

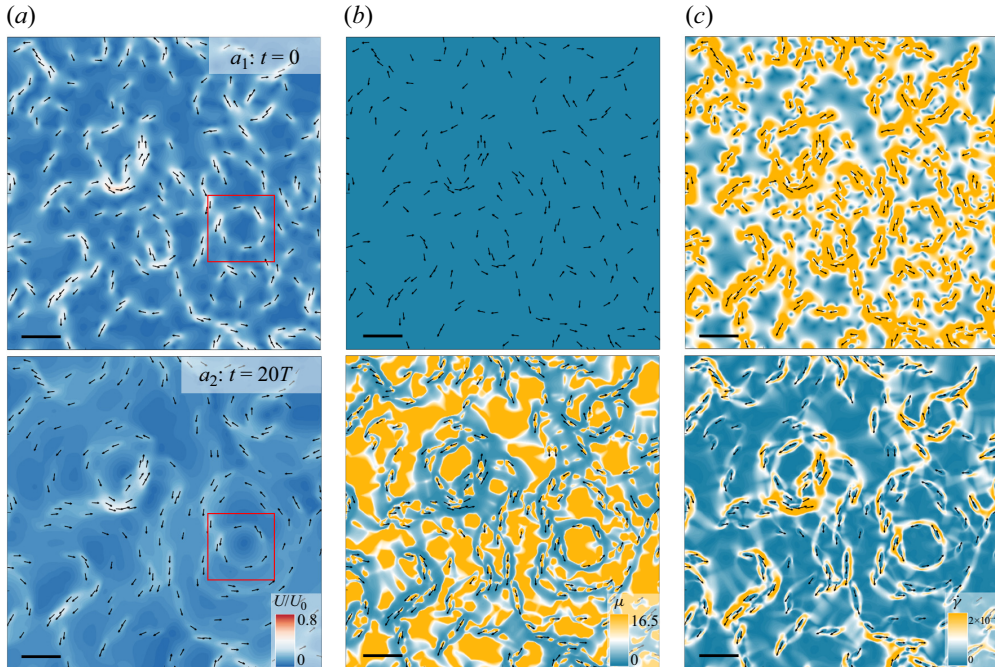


Figure 8. The sequential process of a transition from the PO regime (instant a_1 , $Bn = 0$) to the S regime (instant a_2 , $Bn = 0.15$) by increasing Bn . The steady solution for $Bn = 0$ (instant a_1) is used as the initial condition for the simulation with $Bn = 0.15$. A steady solution for $Bn = 0.15$ is obtained at instant a_2 . Instantaneous contours are coloured by (a) U/U_0 , (b) dynamic fluid viscosity μ (whose value at instant a_1 corresponds to a Newtonian fluid), and (c) local shear-rate magnitude $\dot{\gamma}$ ($\lambda = 1$, $\phi = 0.1$, $n = 1$). Part of the computational domain is shown, and the scale bars correspond to $10D$.

shear, resulting in a decrease in $\dot{\gamma}$ in figure 8(c). At instant a_2 , the low $\dot{\gamma}$ region (blue) corresponding to the high μ region and the non-ciliated region are in solid body rotation or in solid body motion. This solid body rotation has been observed experimentally in the core of swirl by Loiseau *et al.* (2020), visualized in their figures 1(h,i) and their supplementary movies 5 and 6 (available at <https://www.biorxiv.org/content/10.1101/2019.12.16.878108v1.supplementary-material>). The role of the yield stress in generating solid body rotation is that the effective viscosity diverges as the shear rate approaches zero. Here, we examine the distribution of longitudinal velocity u_y in the core of swirls marked in figure 8(a) for $Bn = 0$ and 0.15; u_y is extracted along the red line as schematized in figure 9(a). The distributions of u_y are shown in figures 9(b,c). Here, u_y varies linearly in the radial direction when $Bn = 0.15$, indicating a solid body rotation. This was not reproduced in the previous study (Gsell *et al.* 2020) since a Newtonian fluid was modelled. The addition of the yield stress property to the mucus allows a more accurate modelling of the experiments.

The instantaneous contours of U/U_0 , μ and $\dot{\gamma}$ by increasing Bn from 0.15 to 0.3 are shown in figure 10 ($\lambda = 1$, $\phi = 0.1$, $n = 1$). The steady solution for $Bn = 0.15$ (instant a_2 in figure 8 or instant a_1 in figure 10) is used as the initial condition for the simulation with $Bn = 0.3$. A steady solution for $Bn = 0.3$ is obtained at instant a_3 . The further increase in Bn substantially increases μ at instant a_2 irrespective of the high $\dot{\gamma}$ region at instant a_1 . This further enhances the diffusion of momentum and the coordination of different cilia, resulting in a larger swirl in figure 10(a) (instant a_2). The increase in μ decreases $\dot{\gamma}$, which

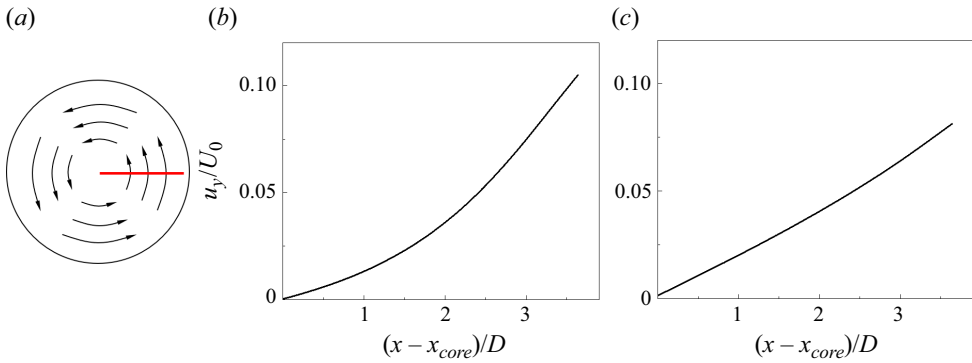


Figure 9. (a) Schematic of velocity extraction in the core of a swirl. Distributions of the longitudinal velocity u_y along the radial direction in the core of swirls marked in figure 8(a), for (b) $Bn = 0$, and (c) $Bn = 0.15$.

in turn increases μ at instant a_3 . Thus there is a positive feedback between the increased μ and the decreased $\dot{\gamma}$ for the flow with yield stress. The S regime gradually converts to the FU regime due to the further diffusion of momentum.

For the regime transition induced by varying n , the instantaneous contours of U/U_0 , μ and $\dot{\gamma}$ by decreasing n from 1 to 0.6 are shown in figure 11 ($\lambda = 1$, $\phi = 0.1$, $Bn = 0$). According to (2.13) and (2.18), the viscosity is $\mu = (\rho U_0^2 \dot{\gamma}^{-1} Re^{-1})(D\dot{\gamma}/U_0)^n$. Here, μ is increased when n decreases from 1 to 0.6 ($D\dot{\gamma}/U_0 < 1$), enhancing the diffusion of momentum and reducing $\dot{\gamma}$. The decrease in $\dot{\gamma}$ in turn leads to an increase in μ due to the shear thinning behaviour. There is also a positive feedback between the increased μ and the decreased $\dot{\gamma}$ for the shear thinning flow. A transition from the PO regime to the S regime is observed at instant a_2 due to the enhanced diffusion of momentum, corresponding to the increase in Λ from 6.36 to 10.15. The effect of shear thinning ($n = 0.6$ and $Bn = 0$) on μ is weak compared to the effect of yield stress ($n = 1$ and $Bn = 0.15$).

Figure 12 shows the instantaneous contours of U/U_0 , μ and $\dot{\gamma}$ by further decreasing n from 0.6 to 0.3 ($\lambda = 1$, $\phi = 0.1$, $Bn = 0$). As mentioned above, the decrease of n leads to the increase of μ . The substantial enhancement of the shear thinning effect significantly enhances the positive feedback between the increased μ and the decreased $\dot{\gamma}$. At instant a_2 , the increase of μ results in the formation of large-scale swirls. At instant a_3 , the further increase of μ and the full coordination of cilia and mucus induce a transition from the S regime to the FU regime. In summary, both the increase of Bn and the decrease of n lead to the successive appearance of PO, S and FU regimes. This is closely related to the increase of μ and the diffusion of momentum. Note that the flow velocities in the ciliated region are lower for the FU regime than for the PO (or S) regime. In the FU regime, the momentum diffuses into the non-ciliated region, and the flow velocity is averaged over ciliated nodes with beating force, and non-ciliated nodes with only friction. In the PO regime, the velocity remains localized above the ciliated region, which is ineffective for the mucus transport.

The variation of $\dot{\gamma}$ directly influences μ under the yield stress and shear thinning effects. Here, we calculate the spatially averaged shear-rate magnitude $\bar{\dot{\gamma}}$ for different cases. The variation of $\bar{\dot{\gamma}}$ as a function of Bn ($\lambda = 1$, $n = 1$) and n ($\lambda = 1$, $Bn = 0$) for different ϕ is shown in figure 13, where $\bar{\dot{\gamma}}$ decreases with increasing Bn and decreasing n , indicating the increase in mucus viscosity. In addition, $\bar{\dot{\gamma}}$ increases with increasing ϕ until $\phi = 0.5$ due to the increase in the number of cilia. The further increase in ϕ significantly enhances the

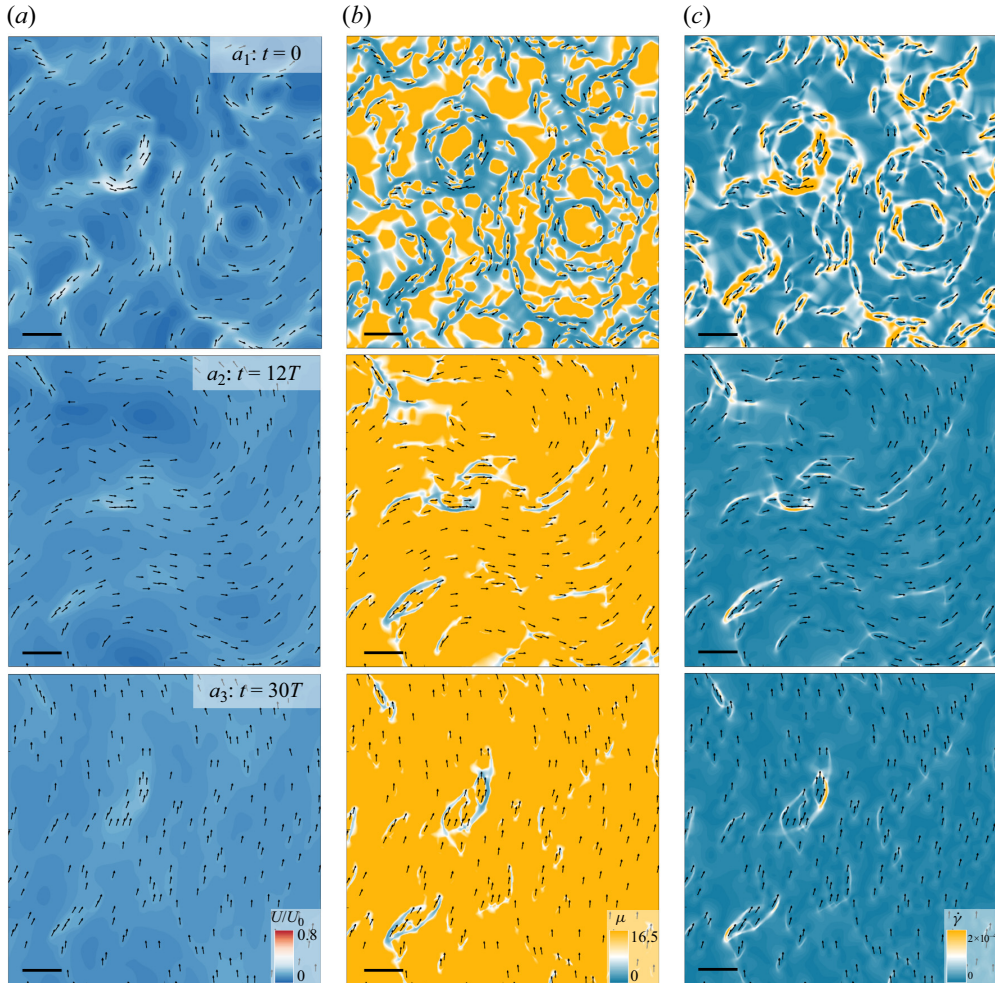


Figure 10. The sequential process of a transition from the S regime (instant a_1 , $Bn = 0.15$) to the FU regime (instant a_3 , $Bn = 0.3$) by increasing Bn : instantaneous contours of (a) U/U_0 , (b) μ , and (c) $\dot{\gamma}$ ($\lambda = 1$, $\phi = 0.1$, $n = 1$). Part of the computational domain is shown, and the scale bars correspond to $10D$.

coordination between different cilia, which tend to beat in the same direction and result in a lower shear. Beyond $\phi = 0.3$, $\bar{\dot{\gamma}}$ is relatively insensitive to the increase in ϕ .

3.4. Effective interaction length

The mucus viscosity μ is the dominant parameter that affects the regime formation when varying Bn and n according to the above discussions. In the present study, the viscosity effect is included in λ , which is defined based on the reference mucus viscosity. To consider the variation of μ , a spatially averaged viscosity $\bar{\mu}$ is calculated for the cases with different Bn and n . The lattice nodes with maximum relaxation time are excluded due to the truncated Herschel–Bulkley law used in the present study. In fact, their viscosity should be considered almost infinite. An effective interaction length λ^* is defined based on $\bar{\mu}$ instead of μ , and λ^* is found to be more suitable to represent the range of influence of the ciliated cells. Figure 14 shows the variation of λ^* as a function of Bn ($\lambda = 1$, $n = 1$) and

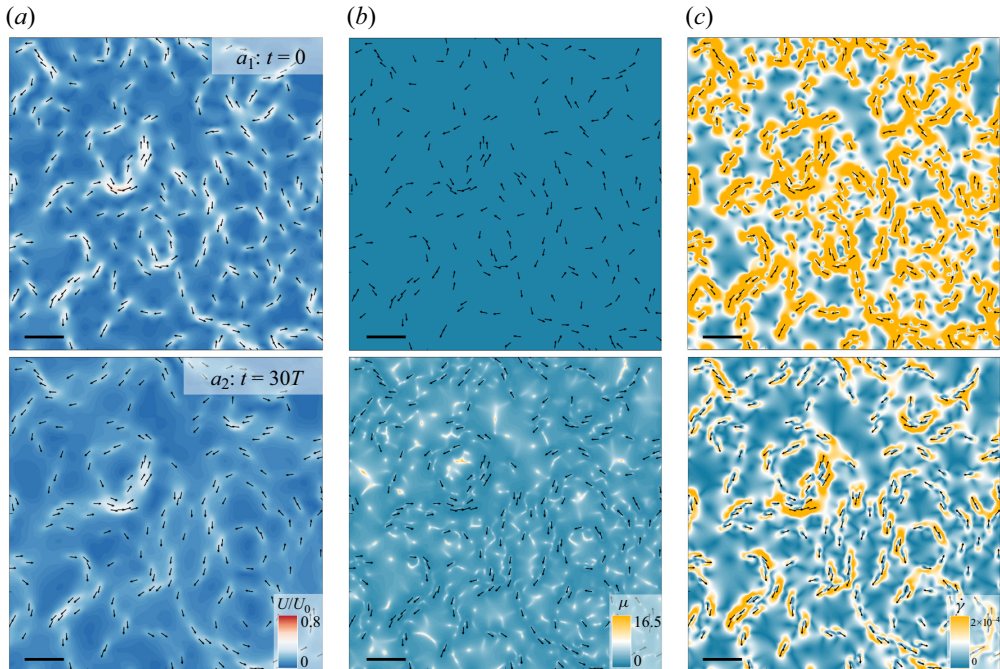


Figure 11. The sequential process of a transition from the PO regime (instant a_1 , $n = 1$) to the S regime (instant a_2 , $n = 0.6$) by decreasing n : instantaneous contours of (a) U/U_0 , (b) μ (whose value at instant a_1 corresponds to a Newtonian fluid), and (c) $\dot{\gamma}$ ($\lambda = 1$, $\phi = 0.1$, $Bn = 0$). Part of the computational domain is shown, and the scale bars correspond to $10D$.

n ($\lambda = 1$, $Bn = 0$) for different ϕ . Here, λ^* increases with increasing Bn and decreasing n , which favours the diffusion of momentum and the coordination between cilia and mucus, thereby resulting in the regime transition. This confirms the results shown in figures 8 and 10–12. For $\phi \geq 0.3$, λ^* is smaller than for $\phi = 0.1$, and the curves of λ^* almost collapse onto a single curve. This corresponds to the variation of $\bar{\gamma}$ in figure 13. Furthermore, the variation of λ^* is opposite to the variation of $\bar{\gamma}$ due to the yield stress and shear thinning effects.

To examine the dependence of the regime formation on λ^* , we compare the variation of \bar{P} as a function of λ and λ^* for different Bn ($\phi = 0.1$, $n = 1$) in figure 15. Recall that to obtain the value of \bar{P} , only the simulations in the most frequent regime have been used. Here, \bar{P} increases with increasing λ , and a rapid increase of \bar{P} can be observed at the critical points for the appearance of the FU regime. The FU regime appears at a smaller λ as Bn is increased. Here, we consider only the critical condition of FU regime formation because the FU regime is the most efficient for mucus transport. The curves of \bar{P} are scattered for different Bn in figure 15(a). In figure 15(b), the curves collapse onto a single curve as a whole for $Bn > 0$. Here, $Bn = 0$ deviates significantly from the collapsed curve; λ^* is not enough to predict the critical condition for different Bn . This may be related to the fact that the increase in Bn leads to a sharp increase in μ , which is truncated when the maximum value is reached.

Figure 16 shows the variation of \bar{P} as a function of λ and λ^* for different n ($\phi = 0.1$, $Bn = 0$). In figure 16(a), the curves of \bar{P} are also scattered, and the critical λ decreases with decreasing n . After the rescaling is performed, the curves collapse onto a single curve as

Hydrodynamic coupling of a cilia–mucus system

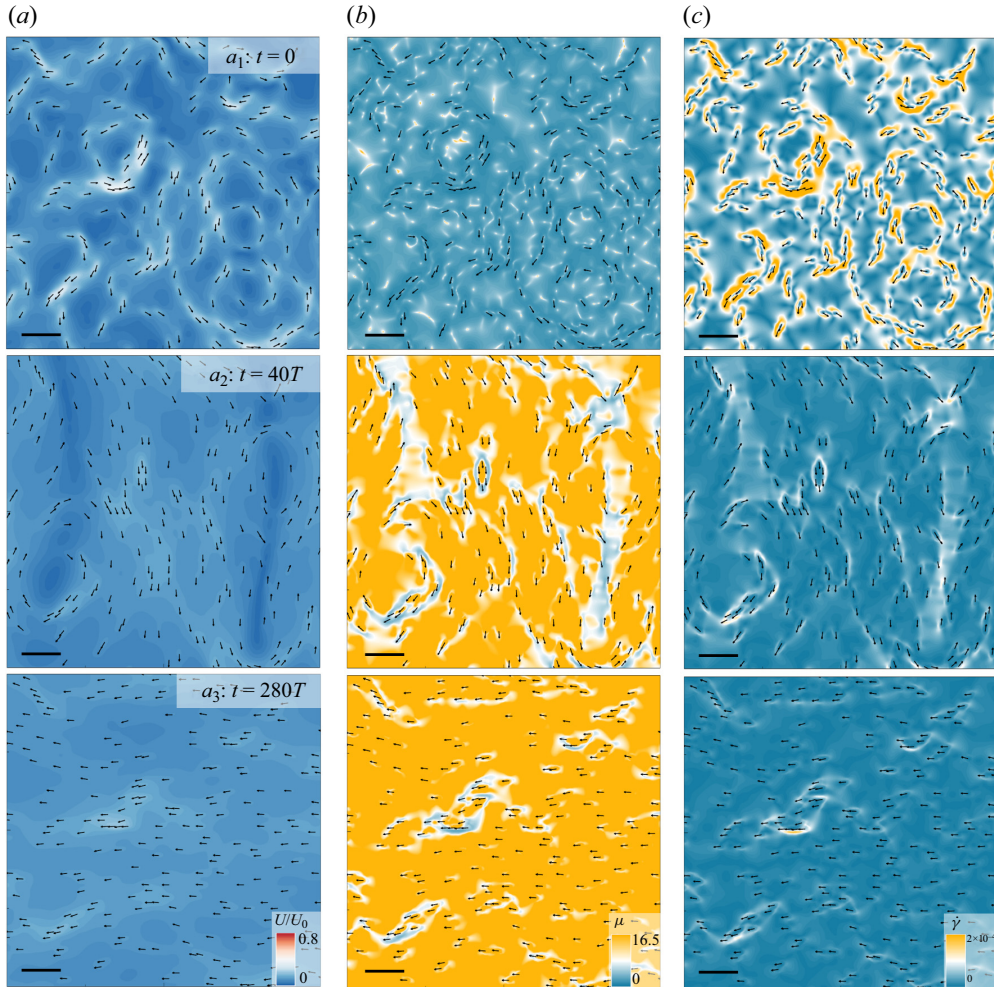


Figure 12. The sequential process of a transition from the S regime (instant a_1 , $n = 0.6$) to the FU regime by decreasing n (instant a_3 , $n = 0.3$): instantaneous contours of (a) U/U_0 , (b) μ , and (c) $\dot{\gamma}$ ($\lambda = 1$, $\phi = 0.1$, $Bn = 0$). Part of the computational domain is shown, and the scale bars correspond to $10D$.

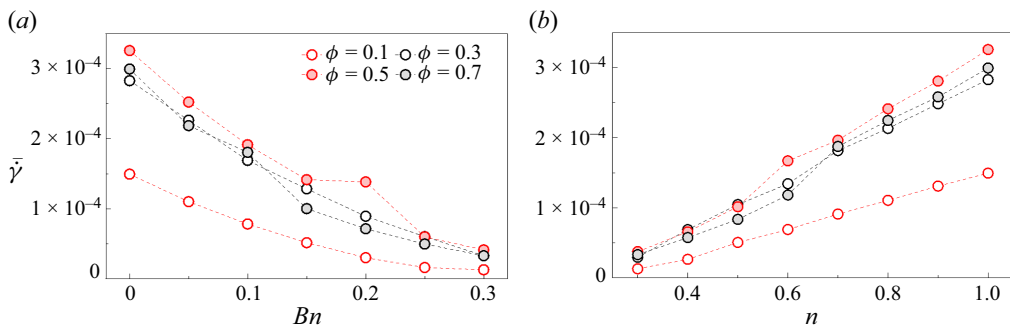


Figure 13. Averaged shear-rate magnitude $\bar{\gamma}$ as a function of (a) Bn ($\lambda = 1$, $n = 1$) and (b) n ($\lambda = 1$, $Bn = 0$), for different ϕ .

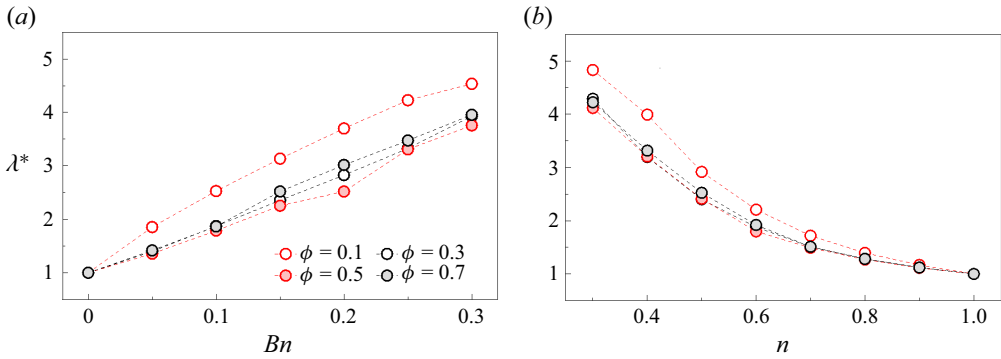


Figure 14. Effective interaction length λ^* as a function of (a) Bn ($\lambda = 1, n = 1$) and (b) n ($\lambda = 1, Bn = 0$), for different ϕ .

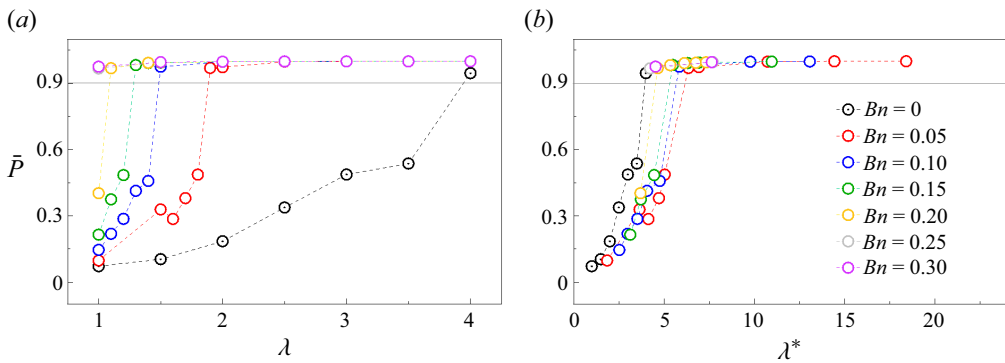


Figure 15. The value of \bar{P} as a function of (a) λ and (b) λ^* , for different Bn ($\phi = 0.1, n = 1$).

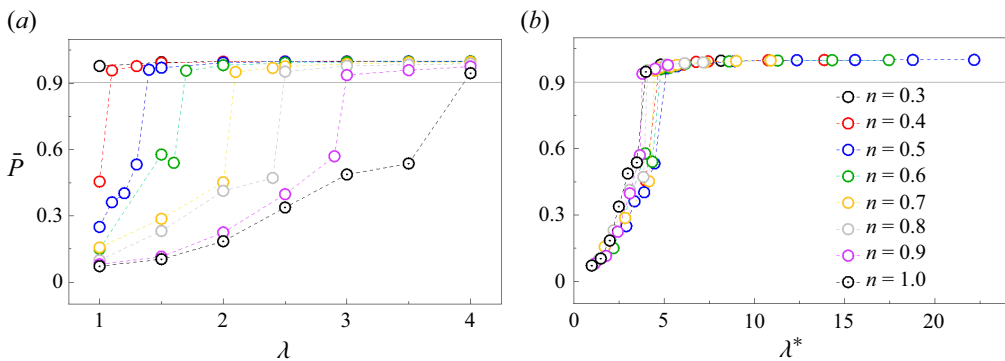


Figure 16. The value of \bar{P} as a function of (a) λ and (b) λ^* , for different n ($\phi = 0.1, Bn = 0$).

a whole. The critical λ^* is distributed in a narrow range $\lambda^* \approx 3.8\text{--}5.1$. Here, λ^* is more suitable for predicting the critical condition of the FU regime formation for different n than that for different Bn .

4. Conclusions




In this work, the hydrodynamic coupling of a cilia–mucus system in Herschel–Bulkley flows was investigated numerically using a two-dimensional hydrodynamic model. The mucus flow was predicted based on the lattice Boltzmann method, and the interaction between the cilia and the mucus was handled by an alignment rule. Numerical simulations were performed in wide ranges of ciliary density (ϕ), interaction length (λ), Bingham number (Bn) and flow index (n) to highlight the effects of yield stress and shear thinning properties on the mucus flow regime. For the effects of ϕ and λ , a poorly organized (PO) regime, a swirly (S) regime and a fully unidirectional (FU) regime were identified. The PO regime appears with low λ and ϕ . The S regime appears with low λ and high ϕ . The FU regime appears with high λ and high ϕ . These are determined by the range of influence of the ciliated cells (range of momentum diffusion) and the coordination between different cilia. For the effects of Bn and n , the range of influence of the ciliated cells is increased by increasing Bn and decreasing n , resulting in the activation of the S and FU regimes at lower ϕ and λ . Mucus viscosity is found to be the dominant parameter affecting the regime formation when varying Bn and n . We define an effective interaction length λ^* based on the spatially averaged viscosity obtained from the final steady solution instead of the reference viscosity, which is more appropriate than λ to represent the range of influence of the ciliated cells. This λ^* increases with increasing Bn and decreasing n , explaining the regime formation upon introduction of Herschel–Bulkley flows. After rescaling, the critical λ^* values for the appearance of the FU regime are still scattered for different Bn , while the critical λ^* values are distributed in a narrow range for different n . So λ^* is more suitable to predict the critical condition of FU regime formation for different n than that for different Bn . Furthermore, the present model is capable of reproducing the solid body rotation observed in experiments, showing a more precise prediction than that of a Newtonian model for the mucus.

Acknowledgements. Centre de Calcul Intensif d’Aix-Marseille University is acknowledged for granting access to its high-performance computing resources. The authors thank Dr S. Gsell for his kind assistance with the code.

Funding. This work was supported by the BonchoClogDrain project (ANR-22-CE30-0045) funded by the French National Research Agency (ANR).

Declaration of interests. The authors report no conflict of interest.

Author ORCIDs.

-  Q. Mao <https://orcid.org/0000-0002-2584-5419>;
-  U. D’Ortona <https://orcid.org/0000-0001-7252-4485>;
-  J. Favier <https://orcid.org/0000-0002-5397-1324>.

REFERENCES

- BANERJEE, R., BELLARE, J.R. & PUNIYANI, R.R. 2001 Effect of phospholipid mixtures and surfactant formulations on rheology of polymeric gels, simulating mucus, at shear rates experienced in the tracheobronchial tree. *Biochem. Engng J.* **7** (3), 195–200.
- BARTON, C. & RAYNOR, S. 1967 Analytical investigation of cilia induced mucous flow. *Bull. Math. Biophys.* **29**, 419–428.
- BLAKE, J. 1972 A model for the micro-structure in ciliated organisms. *J. Fluid Mech.* **55** (1), 1–23.
- BOSELLI, F., JULLIEN, J., LAUGA, E. & GOLDSTEIN, R.E. 2021 Fluid mechanics of mosaic ciliated tissues. *Phys. Rev. Lett.* **127** (19), 198102.
- BRUMLEY, D.R., WAN, K.Y., POLIN, M. & GOLDSTEIN, R.E. 2014 Flagellar synchronization through direct hydrodynamic interactions. *eLife* **3**, e02750.

- BUTTON, B., CAI, L.-H., EHRE, C., KESIMER, M., HILL, D.B., SHEEHAN, J.K., BOUCHER, R.C. & RUBINSTEIN, M. 2012 A periciliary brush promotes the lung health by separating the mucus layer from airway epithelia. *Science* **337** (6097), 937–941.
- CHATEAU, S., D'ORTONA, U., PONCET, S. & FAVIER, J. 2018 Transport and mixing induced by beating cilia in human airways. *Front. Physiol.* **9**, 161.
- CHATEAU, S., FAVIER, J., D'ORTONA, U. & PONCET, S. 2017 Transport efficiency of metachronal waves in 3D cilium arrays immersed in a two-phase flow. *J. Fluid Mech.* **824**, 931–961.
- CHATELIN, R., ANNE-ARCHARD, D., MURRIS-ESPIN, M., THIRIET, M. & PONCET, P. 2017 Numerical and experimental investigation of mucociliary clearance breakdown in cystic fibrosis. *J. Biomech.* **53**, 56–63.
- CHATELIN, R. & PONCET, P. 2016 A parametric study of mucociliary transport by numerical simulations of 3D non-homogeneous mucus. *J. Biomech.* **49** (9), 1772–1780.
- CHILVERS, M.A. & O'CALLAGHAN, C. 2000 Local mucociliary defence mechanisms. *Paediatr. Respir. Rev.* **1** (1), 27–34.
- CHOUDHURY, A., FILOCHE, M., RIBE, N.M., GRENIER, N. & DIETZE, G.F. 2023 On the role of viscoelasticity in mucociliary clearance: a hydrodynamic continuum approach. *J. Fluid Mech.* **971**, A33.
- DING, Y., NAWROTH, J.C., MCFALL-NGAI, M.J. & KANSO, E. 2014 Mixing and transport by ciliary carpets: a numerical study. *J. Fluid Mech.* **743**, 124–140.
- ELGETI, J. & GOMPPER, G. 2013 Emergence of metachronal waves in cilia arrays. *Proc. Natl Acad. Sci.* **110** (12), 4470–4475.
- FAUBEL, R., WESTENDORF, C., BODENSCHATZ, E. & EICHELE, G. 2016 Cilia-based flow network in the brain ventricles. *Science* **353** (6295), 176–178.
- GALKO, A., GSELL, S., D'ORTONA, U., MORIN, L. & FAVIER, J. 2022 Pulsated Herschel–Bulkley flows in two-dimensional channels: a model for mucus clearance devices. *Phys. Rev. Fluids* **7** (5), 053301.
- GINZBURG, I., D'HUMIÈRES, D. & KUZMIN, A. 2010 Optimal stability of advection–diffusion lattice Boltzmann models with two relaxation times for positive/negative equilibrium. *J. Stat. Phys.* **139**, 1090–1143.
- GROTBERG, J.B. 2021 *Biofluid Mechanics: Analysis and Applications*. Cambridge University Press.
- GSELL, S., D'ORTONA, U. & FAVIER, J. 2021 Lattice-Boltzmann simulation of creeping generalized Newtonian flows: theory and guidelines. *J. Comput. Phys.* **429**, 109943.
- GSELL, S., LOISEAU, E., D'ORTONA, U., VIALLAT, A. & FAVIER, J. 2020 Hydrodynamic model of directional ciliary-beat organization in human airways. *Sci. Rep.* **10** (1), 8405.
- GUIRAO, B., *et al.* 2010 Coupling between hydrodynamic forces and planar cell polarity orients mammalian motile cilia. *Nat. Cell Biol.* **12** (4), 341–350.
- GUO, H. & KANSO, E. 2017 A computational study of mucociliary transport in healthy and diseased environments. *Eur. J. Comput. Mech.* **26** (1–2), 4–30.
- HALL, J. & CLARKE, N. 2020 The mechanics of cilium beating: quantifying the relationship between metachronal wavelength and fluid flow rate. *J. Fluid Mech.* **891**, A20.
- HU, S. & MENG, F. 2023 Particle orbiting constrained by elastic filament as a model cilium for fluid pumping. *J. Fluid Mech.* **966**, A23.
- HUSSONG, J., BREUGEM, W.-P. & WESTERWEEL, J. 2011 A continuum model for flow induced by metachronal coordination between beating cilia. *J. Fluid Mech.* **684**, 137–162.
- JORY, M., DONNARUMMA, D., BLANC, C., BELLOUMA, K., FORT, A., VACHIER, I., CASANELLAS, L., BOURDIN, A. & MASSIERA, G. 2022 Mucus from human bronchial epithelial cultures: rheology and adhesion across length scales. *Interface Focus* **12** (6), 20220028.
- JUAN, G.R.R.-S., MATHIJSSSEN, A.J.T.M., HE, M., JAN, L., MARSHALL, W. & PRAKASH, M. 2020 Multi-scale spatial heterogeneity enhances particle clearance in airway ciliary arrays. *Nat. Phys.* **16** (9), 958–964.
- KHELLOUFI, M.-K., LOISEAU, E., JAEGER, M., MOLINARI, N., CHANEZ, P., GRAS, D. & VIALLAT, A. 2018 Spatiotemporal organization of cilia drives multiscale mucus swirls in model human bronchial epithelium. *Sci. Rep.* **8** (1), 2447.
- KIM, Y.W. & NETZ, R.R. 2006 Pumping fluids with periodically beating grafted elastic filaments. *Phys. Rev. Lett.* **96** (15), 158101.
- KNOWLES, M.R. & BOUCHER, R.C. 2002 Mucus clearance as a primary innate defense mechanism for mammalian airways. *J. Clin. Invest.* **109** (5), 571–577.
- KRÜGER, T., KUSUMAATMAJA, H., KUZMIN, A., SHARDT, O., SILVA, G. & VIGGEN, E.M. 2017 *The Lattice Boltzmann Method: Principles and Practice*. Springer.
- LOISEAU, E., GSELL, S., NOMMICK, A., JOMARD, C., GRAS, D., CHANEZ, P., D'ORTONA, U., KODJABACHIAN, L., FAVIER, J. & VIALLAT, A. 2020 Active mucus–cilia hydrodynamic coupling drives self-organization of human bronchial epithelium. *Nat. Phys.* **16** (11), 1158–1164.

Hydrodynamic coupling of a cilia–mucus system

- LU, J., LEI, H., DAI, C., YANG, L. & SHU, C. 2022 Analyses and reconstruction of the lattice Boltzmann flux solver. *J. Comput. Phys.* **453**, 110923.
- MA, J., WANG, Z., YOUNG, J., LAI, J.C., SUI, Y. & TIAN, F.-B. 2020 An immersed boundary–lattice Boltzmann method for fluid–structure interaction problems involving viscoelastic fluids and complex geometries. *J. Comput. Phys.* **415**, 109487.
- MATSUI, H., GRUBB, B.R., TARRAN, R., RANDELL, S.H., GATZY, J.T., DAVIS, C.W. & BOUCHER, R.C. 1998 Evidence for periciliary liquid layer depletion, not abnormal ion composition, in the pathogenesis of cystic fibrosis airways disease. *Cell* **95** (7), 1005–1015.
- MENG, F., BENNETT, R.R., UCHIDA, N. & GOLESTANIAN, R. 2021 Conditions for metachronal coordination in arrays of model cilia. *Proc. Natl Acad. Sci.* **118** (32), e2102828118.
- MESDJIAN, O., WANG, C., GSELL, S., D'ORTONA, U., FAVIER, J., VIALLAT, A. & LOISEAU, E. 2022 Longitudinal to transverse metachronal wave transitions in an *in vitro* model of ciliated bronchial epithelium. *Phys. Rev. Lett.* **129** (3), 038101.
- MITCHELL, B., JACOBS, R., LI, J., CHIEN, S. & KINTNER, C. 2007 A positive feedback mechanism governs the polarity and motion of motile cilia. *Nature* **447** (7140), 97–101.
- MODARESI, M.A. 2023 Numerical investigation of mucociliary clearance using power law and thixotropic mucus layers under discrete and continuous cilia motion. *Biomech. Model. Mechanobiol.* **22** (1), 253–269.
- MORGAN, L., PEARSON, M., DE IONGH, R., MACKEY, D., VAN DER WALL, H., PETERS, M. & RUTLAND, J. 2004 Scintigraphic measurement of tracheal mucus velocity *in vivo*. *Eur. Respir. J.* **23** (4), 518–522.
- NORDGARD, C.T. & DRAGET, K.I. 2011 Oligosaccharides as modulators of rheology in complex mucous systems. *Biomacromolecules* **12** (8), 3084–3090.
- PELLICCIOTTA, N., HAMILTON, E., KOTAR, J., FAUCOURT, M., DELGHEHR, N., SPASSKY, N. & CICUTA, P. 2020 Entrainment of mammalian motile cilia in the brain with hydrodynamic forces. *Proc. Natl Acad. Sci.* **117** (15), 8315–8325.
- QIAN, Y.-H., D'HUMIÈRES, D. & LALLEMAND, P. 1992 Lattice BGK models for Navier–Stokes equation. *Europhys. Lett.* **17** (6), 479.
- SEDAGHAT, M.H., BEHNIA, M. & ABOUALI, O. 2023 Nanoparticle diffusion in respiratory mucus influenced by mucociliary clearance: a review of mathematical modeling. *J. Aerosol Med. Pulm. Drug Deliv.* **36** (3), 127–143.
- SEDAGHAT, M.H., FARNOUD, A., SCHMID, O. & ABOUALI, O. 2022 Nonlinear simulation of mucociliary clearance: a three-dimensional study. *J. Non-Newtonian Fluid Mech.* **300**, 104727.
- SEDAGHAT, M.H., GEORGE, U.Z. & ABOUALI, O. 2021 A nonlinear viscoelastic model of mucociliary clearance. *Rheol. Acta* **60** (6–7), 371–384.
- SHAPIRO, O.H., FERNANDEZ, V.I., GARREN, M., GUASTO, J.S., DEBAILLON-VESQUE, F.P., KRAMARSKY-WINTER, E., VARDI, A. & STOCKER, R. 2014 Vortical ciliary flows actively enhance mass transport in reef corals. *Proc. Natl Acad. Sci.* **111** (37), 13391–13396.
- STAUDT, M.R., ROGALSKI, A., TILLEY, A.E., KANER, R.J., HARVEY, B.-G. & CRYSTAL, R.G. 2014 Tobacco: how it harms us and more reasons to quit: smoking is associated with a loss of ciliated cells throughout the airways. *Am. J. Respir. Crit. Care Med.* **189**, 1.
- TARRAN, R., *et al.* 2005 Normal and cystic fibrosis airway surface liquid homeostasis: the effects of phasic shear stress and viral infections. *J. Biol. Chem.* **280** (42), 35751–35759.
- VASQUEZ, P.A., JIN, Y., PALMER, E., HILL, D. & FOREST, M.G. 2016 Modeling and simulation of mucus flow in human bronchial epithelial cell cultures. Part I. Idealized axisymmetric swirling flow. *PLoS Comput. Biol.* **12** (8), e1004872.
- WANG, C., GSELL, S., D'ORTONA, U. & FAVIER, J. 2023 Generalized-Newtonian fluid transport by an instability-driven filament. *J. Fluid Mech.* **965**, A6.
- WANG, C., TANG, H. & ZHANG, X. 2022 Fluid–structure interaction of bio-inspired flexible slender structures: a review of selected topics. *Bioinspir. Biomim.* **17** (4), 041002.
- WANNER, A., SALATHÉ, M. & O'RIORDAN, T.G. 1996 Mucociliary clearance in the airways. *Am. J. Respir. Crit. Care Med.* **154** (6), 1868–1902.
- WEI, D., DEHNAVI, P.G., AUBIN-TAM, M.-E. & TAM, D. 2019 Is the zero Reynolds number approximation valid for ciliary flows? *Phys. Rev. Lett.* **122** (12), 124502.
- WEI, D., DEHNAVI, P.G., AUBIN-TAM, M.-E. & TAM, D. 2021 Measurements of the unsteady flow field around beating cilia. *J. Fluid Mech.* **915**, A70.
- XU, L. & JIANG, Y. 2019 Mathematical modeling of mucociliary clearance: a mini-review. *Cells* **8** (7), 736.